ELSEVIER

Journal of Non-Crystalline Solids 190 (1995) 264–275

JOURNAL OF NON-CRYSTALLINE SOLIDS

Silica aerogel films at ambient pressure ☆

Sai S. Prakash [a], C. Jeffrey Brinker [a,b,*], Alan J. Hurd [c]

[a] *University of New Mexico / Sandia National Laboratories Advanced Materials Laboratory, Albuquerque, NM 87106, USA*
[b] *Ceramic Synthesis and Inorganic Chemistry Department 1846, Sandia National Laboratories, Albuquerque, NM 87185, USA*
[c] *Ceramic Processing Science Department 1841, Sandia National Laboratories, Albuquerque, NM 87185, USA*

Received 19 May 1995; revised manuscript received 31 May 1995

Abstract

Silica films with refractive indices in the range of 1.006–1.036 (equivalent porosity 98.5–91%) have been prepared at ambient pressure by a process wherein organo-siloxane polymers are deposited on a silicon substrate by conventional dip-coating at 25°C and 0.85 bar (atmospheric pressure in Albuquerque) and heating to 450°C. The film thicknesses (from scanning electron microscopy) vary from 0.1 to 3.5 μm, depending upon the dip-coating rate (0.05–1.9 cm/s) and concentration of the sol. The process was optimized by varying the dilution, aging, organic modification, heat treatment and dip-coating conditions, allowing control of film porosity in the range ~30–99%. Imaging ellipsometry has been used to study the evolution of film porosity and thickness in situ. It is observed that the high porosity in these films is mainly attributable to dilation or 'springback' of the film during the final stage of drying.

1. Introduction

The extraordinary properties of aerogels including high surface areas (often $> 1000\ m^2/g$), low refractive indices (< 1.1), low dielectric constants (< 1.7), low thermal loss coefficients ($< 0.5\ W/(m^2\ K)$ and low sound velocities ($< 100\ m/s$) lead to potential thin film applications such as: ultra-low dielectric constant interlayer dielectrics, reflective and anti-reflective coatings, flat panel displays, sensors, superinsulated architectural glazing and acoustic impedance matching. To date, however, the potential of aerogels in thin film applications has not been realized, mainly because conventional supercritical aerogel processing is very energy intensive, often dangerous, and most importantly — not easily adaptable to continuous thin film forming operations such as dip-coating. [1] The ambient-pressure route overcomes these problems, enabling the preparation of thin film specimens in a continuous process, previously impossible to do within the constraints of an autoclave.

In 1931, Kistler demonstrated the preparation of aerogels by supercritical extraction of the pore fluid from a wet gel [2]. Under supercritical conditions, the drying stress, P_C, exerted by the liquid on the gel network is essentially zero (since liquid–vapor interfaces are eliminated), often causing little or no shrinkage during drying [3]. In 1992, Deshpande et

☆ Presented at the 4th International Symposium on Aerogels, Berkeley, CA, USA, 19–21 September 1994.

* Corresponding author. Tel: +1-505 272 7627. Telefax: +1-505 272 7304. E-mail: jbrinker@unm.edu.

[1] Conventional aerogel films were prepared in a batch process by Hrubesh and Poco [1].

SSDI 0022-3093(95)00024-0

al. used an alternate route to prepare *bulk* aerogels at ambient pressure [4]. In the ambient pressure process, the maximum drying stress is finite ($|P_C| = 2\gamma_{LV} \cos\theta/r_P > 0$, where γ_{LV} is the surface tension, θ is the contact angle and r_p is the pore radius) [5], but, due to organic modification of the internal gel surface, drying-related shrinkage is almost completely reversible.

This paper extends previous work on the preparation of bulk aerogels [4,6] to the preparation of thin films using an ambient pressure process. Imaging ellipsometry is used to monitor the film deposition process in situ [7,8]. We observe that the $>90\%$ film porosity is attributable to stress relaxation or 'springback' of the film during the final stage of drying.

2. Experimental

2.1. Optimized preparation and characterization

Silicate sols were prepared from tetraethoxysilane (TEOS) dissolved in ethanol using a two-step acid/base catalyzed procedure (referred to as B2) [3]. In the first step, TEOS, EtOH, H_2O and HCl were combined in the molar ratios $1.0:3.8:1.1:7.0 \times 10^{-4}$ and refluxed at 60°C for 90 min (stock solution). In the second step, 0.05M NH_4OH, stock solution and EtOH were combined in the volume ratios $1:10:11r_E$. r_E denotes the ethanol-dilution ratio [2] and was varied over the range (0–5). The B2 sols were allowed to gel and age at 50°C. The relative aging time, t/t_{gel} [3], was varied between 1 and 3.6.

The gels were then subjected to a pore fluid-exchange procedure using hexane, and the surface hydroxyls were partially replaced with organosilicon groups using a silylation procedure [9]. The details of this step are presented elsewhere [10]. The extent of surface modification (that is equal to the percent of hydroxyls replaced, determined by ^{29}Si NMR) was varied between 0 and $\sim 25\%$ (c_M), using different concentrations of the modifying reagent (0–7% solution in hexane).

The surface-modified gels were reliquified using ultrasound (20 kHz frequency, ~ 95 W power). The concentration of the redispersed sol was controlled by addition of hexane. An optimization study was conducted on the sonication time, t_{son}, needed to give the most porous films. The sols were characterized using ^{29}Si nuclear magnetic resonance (NMR) (Chemagnetics 200 NMR) and Fourier-transform infrared (FTIR) spectroscopy (Magna-IR spectrometer) [11].

The reliquified sols were dip-coated onto Si substrates, at speeds varying from 0.05 to 1.9 cm/s. The freshly coated films were heated to different temperatures in the range 30–750°C at varying heating/cooling rates (1°C/min, 10°C/min, infinite [4]). The dipping speed and pyrolysis temperature were optimized for maximum film porosity (V_d and T_{max}, respectively). For the optimization studies, ellipsometry (Gærtner Scientific Corporation Model L116C) was used to determine the refractive index and thickness of the films. The refractive index values presented in plots in Section 3 denote averaged values (at least five to six points were measured on each film). The Lorentz–Lorenz equation was used to relate refractive index to vol.% porosity, assuming a skeletal refractive index of 1.46 [3]. Films deposited on Si substrates were also characterized by FTIR and SEM (Hitachi model S-800) to determine compositional information and observe film thickness and cracking behavior, respectively. A surface acoustic wave (SAW)-based N_2 sorption technique [12] utilizing a Micromeritics ASAP 2000 instrument was employed to determine film pore volume and surface area. To obtain NMR data on the aerogels, thin layers of sol were cast in a petri dish, allowed to dry at room temperature and analyzed by solid-state magic angle spinning ^{29}Si NMR spectroscopy to quantify the distribution of tetrafunctional (Q) and proportion of monofunctional (M) Si species.

2.2. In situ characterization by ellipsometric imaging

In order to observe the evolution of film porosity, the film deposition process was studied in situ using

[2] r_E = volume ethanol/volume (stock + NH_4OH).

[3] t/t_{gel} = total (gelation + aging) time/gelation time.

[4] The samples were directly placed in the oven pre-heated to its maximum temperature.

a home-made broad-beam ellipsometric imaging setup shown schematically in Fig. 1 [7,8]. The ellipsometer consisted of a polarizer-compensator-sample-analyzer (PCSA) arrangement of optical elements followed by a charge coupled detector (CCD) camera to record the process. An ~1 cm diameter spot of polarized light from a He–Ne laser source ($\lambda = 6328$ Å) was used to illuminate the steady-state depositing film near the drying line, incident at 67.5°. The polarization change suffered upon reflection and refraction from the drying film was analyzed from the recorded images to quantify the refractive index and film thickness profiles near the drying line. Changes in the film thickness and refractive index give rise to interference fringes and these were observed visually on a TV monitor for qualitative information. The photometric detection method [13], which is briefly described in the next section was used for profiling. For the ellipsometric imaging experiments, hexane was replaced by ethanol, due to the latter's lower volatility. This replacement does not affect the sol chemistry significantly, as determined using ^{29}Si NMR. Image analysis was performed using Image 1.49 VDM and Screenplay II software.

2.2.1. Refractive index and thickness profiling by photometric detection

As opposed to null ellipsometry, photometric detection involves the measurement of light intensity profiles from the recorded images that depends on the ellipsometric parameters Ψ and Δ and the settings of the optical elements. With the polarizer angle P, set at 0° and the compensator, C, at 45°, the polarization change upon interaction with the forming film was analyzed at various positions of the analyzer, A. The linear region of the alternating intensity versus A curve was chosen suitably, and the position-dependent intensity profiles, $I(x)$, were obtained for $A = -90$, -120 and $-135°$. These profiles were used to obtain the ellipsometric parameters, $\Psi(x)$ and $\Delta(x)$, which were converted to refractive index, $n(x)$, and thickness, $h(x)$, profiles using standard ellipsometric equations and plots [11].

Assuming the compensator to behave as an ideal quarter-wave plate, and setting $P = 0°$, $C = 45°$, intensity at any point on the image is given by

$$I = C_1 |[\tan \Psi \cos A(\cos \Delta + \sin \Delta) + \sin A] - j[\tan \Psi \cos A(\cos \Delta - \sin \Delta) - \sin A]|^2$$

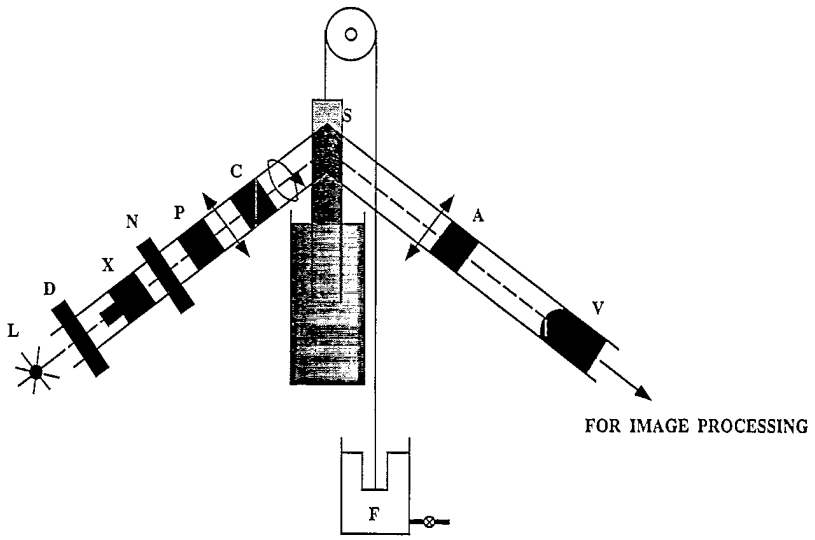

Fig. 1. Schematic of imaging ellipsometry apparatus used for analysis of film deposition in situ. L: He–Ne laser source; D: depolarizer; X: beam-expander; N: diffusing screen; P: polarizer; C: compensator; S: sample; A: analyzer; V: video camera; F: float. Light exiting the polarizer and compensator are linearly and circularly polarized respectively.

$$= 2C_1\left[\tan^2\Psi + (1-\tan^2\Psi)\sin^2 A + \tan\Psi \sin\Delta \sin 2A\right], \quad (1)$$

where C_1 is a parameter independent of P, C and A. Normalizing with respect to the intensity at $-90°$,

$$i = \frac{I}{-I_{90°}} = \tan^2\Psi + (1-\tan^2\Psi)\sin^2 A + \tan\Psi \sin\Delta \sin 2A. \quad (2)$$

Thus, for any two analyzer settings A_i and A_k, Ψ and Δ can be deduced as

$$\tan^2\Psi = \frac{\sin 2A_k(i_i - \sin^2 A_i) - \sin 2A_i(i_k - \sin^2 A_k)}{\cos^2 A_i \sin 2A_k - \cos^2 A_k \sin 2A_i} \quad (3)$$

$$\tan\Psi \sin\Delta = \frac{\cos^2 A_i(i_k - \sin^2 A_k) - \cos^2 A_k(i_i - \sin^2 A_i)}{\cos^2 A_i \sin 2A_k - \cos^2 A_k \sin 2A_i}. \quad (4)$$

The $\Psi(x)$ and $\Delta(x)$ profiles were converted to refractive index, $n(x)$, and thickness, $h(x)$, profiles [11]. In plotting the film thickness profile, the true thickness was deduced as the sum of the calculated first phase thickness (from Ψ and Δ) and the fringe number times the phase thickness multiple, i.e.,

h = calculated thickness + (fringe number × phase thickness).

2.2.2. Concentration profiling

The volume fraction solid, ϕ_S, liquid, ϕ_L, and gas, ϕ_G, profiles can be deduced from $n(x)$ and $h(x)$ via the following models:

$$h(x)\phi_S(x) = \text{constant}, \quad (5)$$

$$\frac{n(x)^2 - 1}{n(x)^2 + 2} = \phi_S(x)\frac{n_S^2 - 1}{n_S^2 + 2} + \phi_L(x)\frac{n_L^2 - 1}{n_L^2 + 2}, \quad (6)$$

$$\phi_G(x) = 1 - \phi_S(x) - \phi_L(x). \quad (7)$$

Eq. (5) follows from mass balance arguments and assumes the volume of solids is a constant. This is a reasonable assumption in the post-gelation stage where all of the silica exists in a condensed state. Eq. (6) (the Lorentz–Lorenz model) relates the measured refractive index, n, to the refractive index of the solid, n_S, and liquid, n_L, components of the sol or gel assuming spherical inclusions of liquid or gas within a solid matrix. n_S (silica) = 1.46, n_L (ethanol) = 1.36, n_L (water) = 1.33. Porosity (ε) can be defined as

$$\varepsilon(x) = \phi_L(x) + \phi_G(x) = 1 - \phi_S(x). \quad (8)$$

3. Results

3.1. Parameter variation study

The experimental matrix of the optimized method of preparation of aerogel thin films is shown in Fig. 2. Figs. 3(a) and (b) relate the effect of the extent of surface silylation on the final refractive index of films heated to 450°C for 1 h. Fig. 3(a) shows the extent of organic modification in terms of the vol.% silylating reagent used versus refractive index, while Fig. 3(b) shows the quantified extents of silylation, M and the Q-distributions (determined by solid-state ^{29}Si NMR) as a function of final refractive index. Smooth curve fits were applied to the data, as a guide to the eye. The film refractive index decreased with vol.% silylating reagent up to about 6%, beyond which cracking and an increase in refractive index were observed.

Fig. 4 shows the influence of (a) aging and (b) temperature on the refractive index of the films. In the aging plot (both as-deposited films and films heated to 450°C are shown), the optimized extent of organic modification was used and third-order polynomial fits were applied to the data. The refractive index decreases with aging time for both as-deposited and heated films, but flattens out faster in the latter case. In the temperature plot (Fig. 4(b)), the refractive index is plotted versus heat treatment temperature for films prepared using optimized values of the extent of organic modification and aging time. Smooth curve fits were applied to the data. Increasing temperature causes the refractive index to decrease, level off in the range ~ 450–650°C, and then to increase.

The influence of dip-coating speed and sonication time were also studied and details of these and other optimization steps are presented elsewhere [10]. It

was observed that the refractive index decreased with dip-coating speed and increased with sonication time.

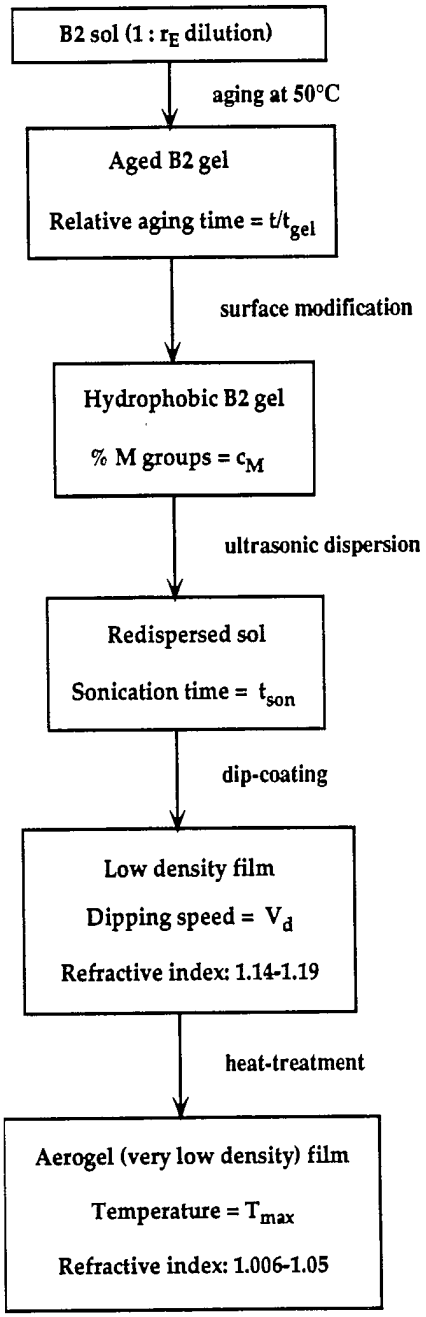

Fig. 2. Schematic of experimental matrix used for the optimized preparation of aerogel thin films. r_E, t/t_{gel}, c_M, t_{son}, V_d and T_{max} denote the variables optimized to give most porous films.

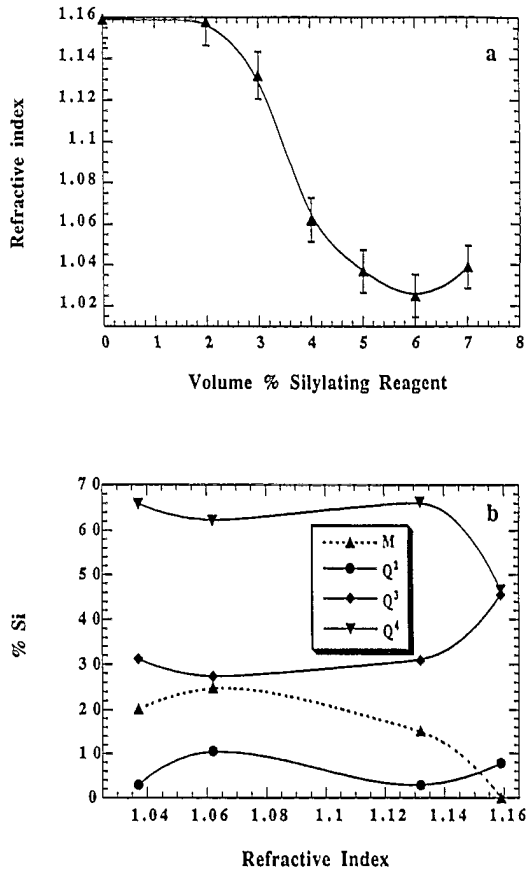

Fig. 3. Influence of organic modification on refractive index (films heated to 450°C for 1 h). (a) Vol.% silylating reagent in hexane versus refractive index, (b) Q and M distributions (from ^{29}Si NMR) versus refractive index.

3.2. Characterization

3.2.1. Surface acoustic wave (SAW)-based gas sorption experiments [12]

Fig. 5 shows (a) a sorption isotherm of a film prepared by the exact same process as shown in Fig. 2 without the surface modification step (this sample is identified as 'X-film' and has a porosity of ~ 60%); (b) a sorption isotherm of a corresponding aerogel film (porosity > 90%); and (c) the pore size distribution of the aerogel film, determined from the adsorption and desorption branches of Fig. 5(b). The data were obtained on an areal basis (also see Table 1). For approximate comparisons with bulk aerogels, these were converted to a per gram basis using film

thickness (~ 0.18 μm) and skeletal density (~ 2.1 g/cm^3) values. Similar data on ambient-pressure bulk aerogels (reproduced from Ref. [6]) are presented in Table 1 for comparison.

3.2.2. Scanning electron microscopy (SEM)

Scanning electron microscopy supplemented ellipsometric information on film thickness. By varying sol concentration prior to coating or substrate withdrawal rate or both, aerogel films of thickness in the range 0.1–3.5 μm were prepared. Fig. 6 shows an edge-on view of a crack-free 1.8 μm thick aerogel film.

3.2.3. Fourier-transform infrared (FTIR) spectroscopy

Transmission FTIR spectroscopy of surface-modified sols indicated the presence of silanol groups at much reduced concentration relative to the non-modified sols (X-sols) [11]. Fig. 7 shows FTIR spectra of four samples: (a) an as-deposited aerogel film at

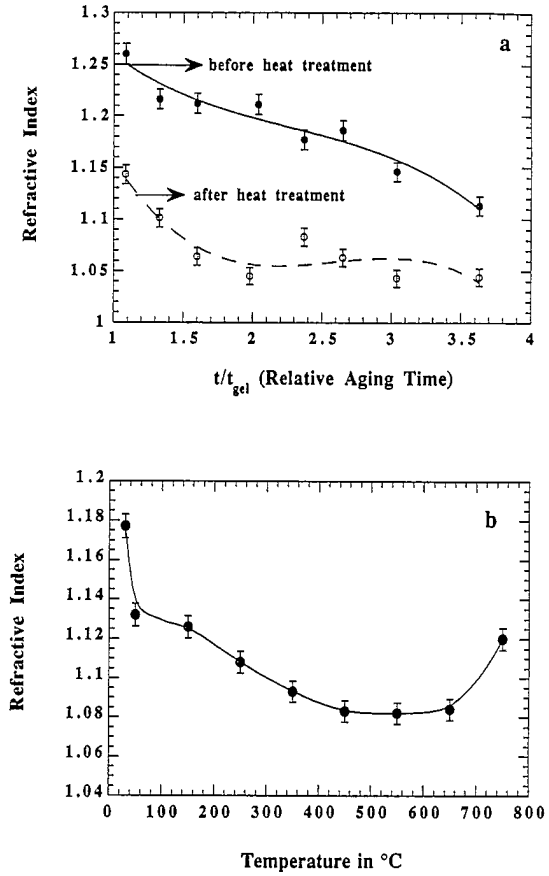

Fig. 4. (a) Influence of aging time on refractive index (third-order polynomial fits applied to data) for as-deposited and 450°C-treated films. (b) Influence of pyrolyzing temperature on refractive index.

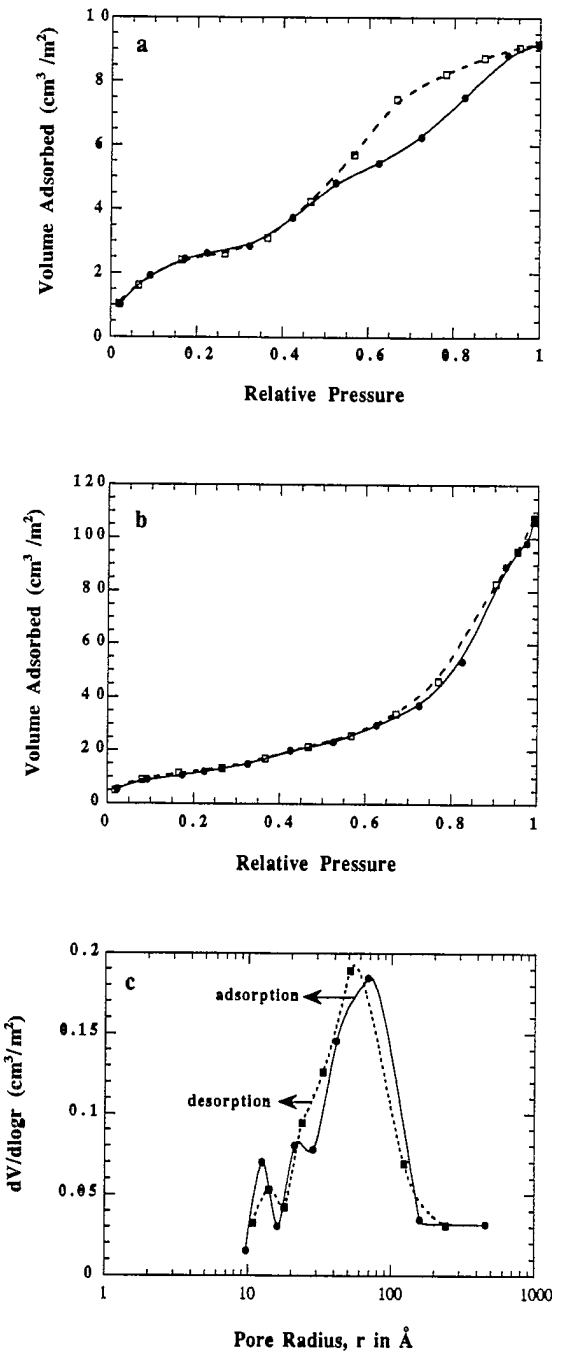

Fig. 5. Sorption results. (a) Sorption isotherm of X-film. (b) Sorption isotherm of aerogel film. (c) Pore size distribution of aerogel film, (units are on areal basis).

Table 1
Pore volume and surface area measurements from nitrogen-sorption experiments

Property of ambient pressure aerogel	Film (per m^2 basis) (measured)	Film (per g basis) (calculated)	Bulk (per g basis) (literature [6])
BET surface area	43 m^2/m^2	~ 1140 m^2/g	869 m^2/g
BJH pore volume	0.163 cm^3/m^2	~ 4.3 cm^3/g	3.1 cm^3/g

room temperature, (b) an aerogel film heated to 150°C, (c) an aerogel film heated to 450°C and (d) an X-film heated to 150°C for comparison. Of particular interest are spectral regions centered at 3450 (SiO ↔ H), 2960, 1170 and the 980 cm^{-1}. The 1170 and 980 peaks indicate the presence of ethoxy groups [14]. The absence of silanol groups in (a) and (b) and the hint of their reappearance in (c) correlates with the presence of ethoxy groups in (a) and (b) and their diminution in (c). Also, note that in (d), substantial

Fig. 6. Cross-sectional SEM micrograph of a 1.8 µm thick aerogel film.

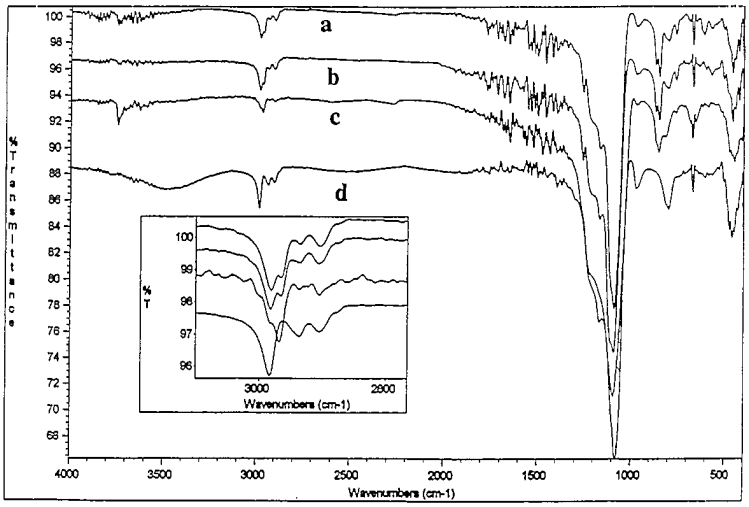

Fig. 7. FTIR spectra of (a) as-deposited aerogel film, (b) 150°C-treated aerogel film, (c) 450°C aerogel film and (d) 150°C-treated X-film. Inset: Magnified view of spectra around the C–H vibrations zone.

hydroxyls are present despite condensation reactions that occur during film formation. The inset indicates an enlarged view of the C–H region ($\sim$ 2900–2980 cm^{-1}).

3.2.4. Nuclear magnetic resonance (NMR) spectroscopy

Fig. 8 shows superimposed solid-state ^{29}Si NMR spectra of xerogel samples corresponding to the aerogel film (a) and the X-film (b). The organosilicon content, M, was $\sim 20\%$ for the films that had $> 90\%$ porosity, while the X-films (no organic modification) had $\sim 60\%$ porosity. It is worthwhile to note that, compared with the X-gel, the Q^2 and Q^3 resonances are diminished for the surface-modified gel, and new resonances appear in the ~ 15 ppm zone associated with silicon nuclei bonded to one bridging oxygen (referred to as M units). The inset

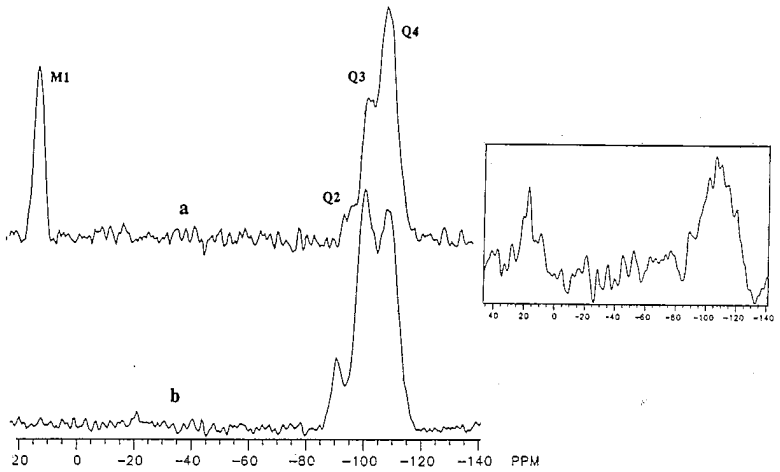

Fig. 8. Solid-state ^{29}Si NMR spectra of (a) sol used to prepare aerogel film, (b) X-sol. Inset: Liquid-state ^{29}Si NMR spectrum of ethanol-based sol used for imaging ellipsometry studies.

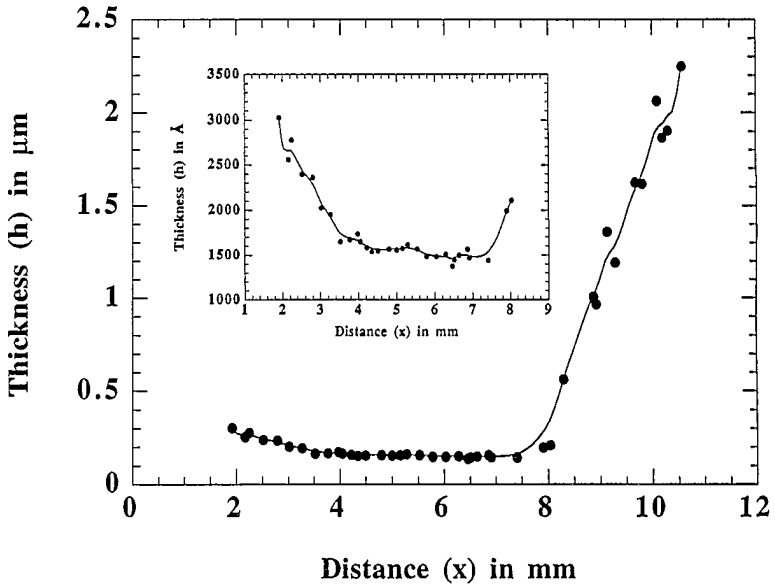

Fig. 9. Thickness profile of aerogel film. Inset: Magnified view near 'springback' zone.

is the liquid-state ^{29}Si NMR spectrum of the ethanol-based sol used to prepare the sample corresponding to Fig. 8(a). As mentioned in Section 2.2., the pore fluid replacement of hexane by ethanol has little influence on the sol chemistry.

3.2.5. Imaging ellipsometry

Fig. 9 shows the film thickness profile in an ~ 1 cm region around the drying line, while the inset shows the same magnified in the vicinity of the drying line. The drying line is arbitrarily defined as

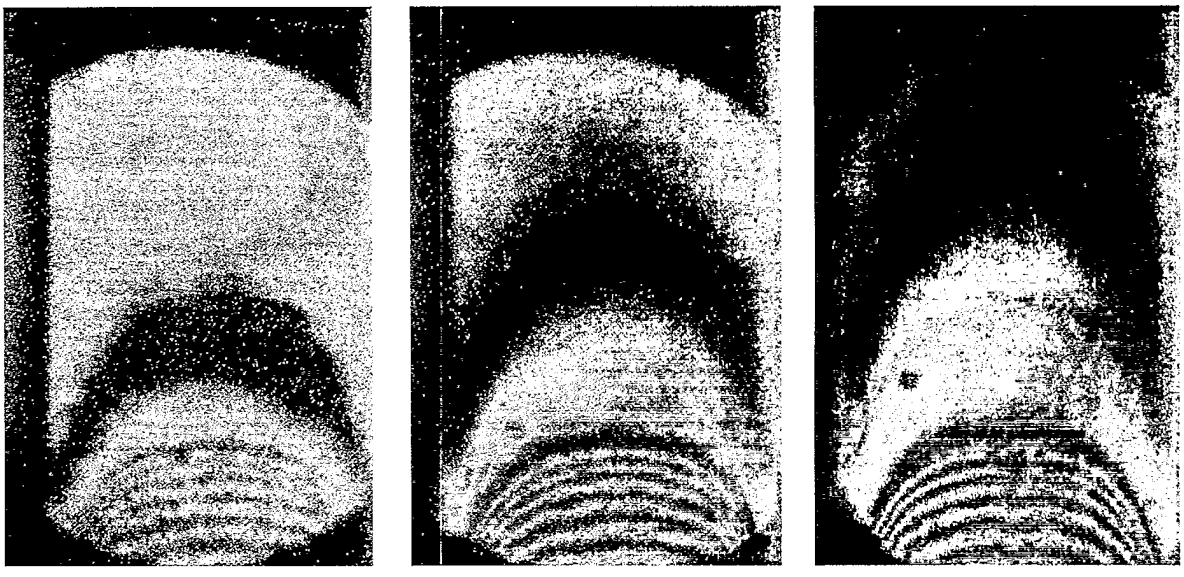

Fig. 10. Frames of recorded images with increasing analyzer position. The broad fringes indicate the gradual change in film thickness in the 'springback' zone, while the narrow fringes indicate the sharp change in film thickness in the compaction zone.

the line where the gradient in film thickness or alternatively the evaporation rate is maximum. The origin in these plots (and Fig. 11) is arbitrarily fixed at some reference point in the steady state image. The most significant feature of this figure is that the film rapidly shrinks as it approaches the drying line and then, after it has reached its point of maximum compaction, which corresponds to the complete development of liquid–vapor menisci, 'springs back' to about twice the thickness of the compacted state.

'Springback' was proven qualitatively and unambiguously by observing the direction of fringe-shift upon gradually changing the optical setting [15]. The presence of interference fringes indicates a gradient in film thickness and/or refractive index. The narrower the fringes are, the steeper the gradient. With the polarizer and compensator fixed, the analyzer was rotated over a small range, and frames of the images at analyzer settings of -90, -120 and $-150°$ were 'grabbed' for analysis. The images (Fig. 10) showed that the narrow fringes moved downward while the broad fringes moved upward as A was progressively rotated from $-90°$ to $-150°$. The movement of the narrow fringes though subtle in observation of the images was distinct when the intensity profiles were plotted [15]. This relative fringe movement in opposite directions about the drying line indicated the presence of a valley in film thickness in that region, on either side of which the film thickness increases.

Fig. 11 shows (a) the measured refractive index profile, $n(x)$, for the aerogel film, and (b) the calculated porosity profile, $\varepsilon(x)$, obtained from the film thickness profile, using Eqs. (5) and (8). At >10 mm the pores are largely liquid-filled, while at <2 mm they are largely gas-filled. The final refractive index and thickness measured by the above method were in good agreement with those measured using a commercial ellipsometer. For comparison, a similar experiment was conducted on an X-film. It showed a fringe pattern typical of a parabolic thickness profile, with no change in film thickness and refractive index above the drying line [15], and upon rotation of A, the fringes moved unidirectionally.

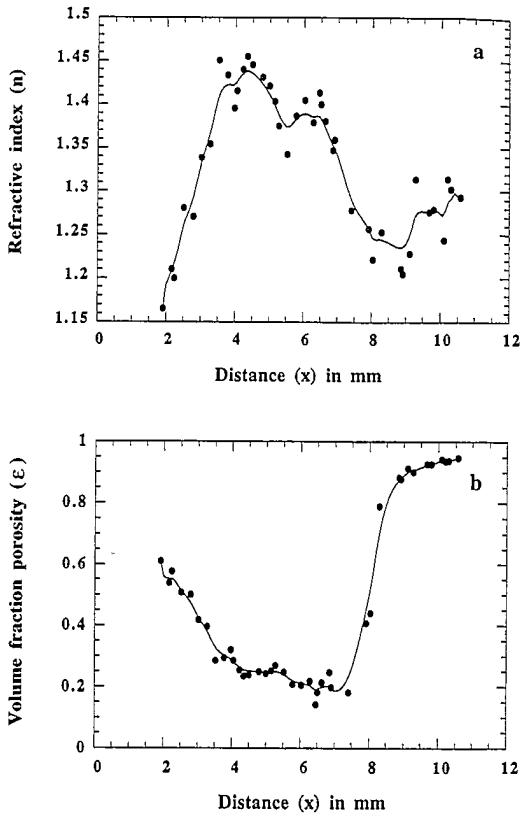

Fig. 11. (a) Refractive index profile. (b) Porosity (liquid+vapor volume fractions) profile obtained from the film thickness profile. At >10 mm, the pores are largely liquid-filled, while at <2 mm they are largely gas-filled.

4. Discussion

Imaging ellipsometry clearly showed that during the ambient pressure process, the gel network is subjected to a capillary stress causing it to compact. The compaction is followed by 'springback' at the final stage of drying corresponding to elimination of liquid-vapor menisci, and hence the drying stress. Film porosity is expected to be maximized therefore under conditions that minimize (i) capillary pressure, (ii) compaction of the gel network, and (iii) skeletal density, and maximize 'springback'. The variables listed in Fig. 2 can be discussed in this context.

As observed for bulk aerogels, we believe the effect of aging is to strengthen the primary structural units comprising the sol, causing the ensuing gel network to better withstand the capillary stress to

which it is subjected during drying. The effect of dip-coating speed can be rationalized on a similar basis. Higher speeds increase the film thickness and protract the drying time. This is analogous to an increase in aging time. We speculate that the optimum in sonication time may reflect a trade-off between the size-dependent density and elastic moduli of fractal clusters identified by small angle X-ray scattering on the 5–350 Å length scale [10]: increasing cluster size causes both cluster density and modulus to decrease.

Combined thermogravimetric analyses, FTIR and ellipsometry results indicate that the effect of heating to 450°C is to oxidize residual organic groups, both ethoxide and organosilanes, creating a more porous network [11]. FTIR shows that pyrolysis transforms the largely hydroxyl-free, hydrophobic surface to a hydroxylated, hydrophilic surface as noted by a reduction in the relative intensities of ethoxide vibrations (1170 and 980 cm^{-1}) and C–H stretching vibrations ($\sim$ 2900–2980 cm^{-1}) and the appearance of O–H stretching vibrations at 3400–3700 cm^{-1}.

Comparison of the ^{29}Si NMR and FTIR results indicate that, although the extent of surface modification is not complete (there remains $\sim$ 27% of silicon as $Q^2 + Q^3$ species), the non-modified sites in the aerogel films are largely ethoxylated, since the absorption in the O–H stretching region is very low for the as-deposited and 150°C-treated films. Hydroxyl groups present in the sols apparently undergo condensation during film formation.

The most remarkable feature of ambient-pressure aerogel film formation, namely, 'springback', is attributed to the capping-off of reactive terminal hydroxyl groups with organosilane ligands that cannot participate in condensation reactions. In this situation, drying shrinkage is largely reversible. Other workers [4,16] have observed a similar effect in bulk ambient-pressure aerogels. 'Springback' is shown to approximately double the thickness of the most fully compacted film state. Analysis of the accompanying change in porosity indicates that this corresponds to a porosity increase of at least 200%. In situ imaging ellipsometry of the X-sol during film deposition indicates that for non-modified siloxanes, the shrinkage process is completely irreversible.

Interpretation of $n(x)$ and $h(x)$ together using Eqs. (5)–(8) points to a poorly understood feature of sol–gel dip-coating that requires further study. The data indicate a local maximum in the liquid fraction profile, $\phi_L(x)$, at $\sim$ 3.5 mm. In other words, moving from right to left on the plots, the liquid content in the film reaches a minimum near the drying line ($\sim$ 7.2 mm), then increases from $\sim$ 7.2 to 3.5 mm, and then decreases again to the final dry state. The cause for this behavior is unclear, but is expected to be due to a competition between liquid loss by evaporation and liquid influx via Darcy flow caused by a two-dimensional (substrate velocity and film thickness dimensions, x and h, respectively) variation of capillary pressure, P_C. The data rightly point to low liquid concentrations in regions where the evaporation rate ($\propto dh/dx$) is high, and high liquid concentrations in regions where the two-dimensional Darcy flux ($\propto \nabla P_C$) is expected to be maximized. Other possible causes are surface tension gradient-driven flows or a change in wetting characteristics due to the presence of water, in the final stages of drying, within a hydrophobic environment.

5. Conclusions

Films with aerogel-like properties (volume fraction porosity > 90%) can be prepared at ambient pressure, by a simple dip-coating procedure followed by a low-temperature heat treatment. Considerable porosity is created by dilation or 'springback' of the film upon elimination of the capillary pressure at the final stage of drying. 'Springback' is a general phenomenon and it may accompany drying in a variety of sol–gel systems, where β-diketonates, alcohol amines and carboxylic acids are used to 'cap-off' reactive hydroxyl ligands.

The authors thank Donald Stuart for his assistance with the imaging ellipsometry setup, S. Prabhakar for the NMR spectra, Teresa Bohuszewicz and Stephen Wallace for the SAW-sorption results, Laurent Delattre for the FTIR spectra and Mei Qiu for the SEM pictures. This work was supported by the US Department of Energy Basic Energy Sciences program under contract number DE-AC04-94 AL 85000.

References

[1] L.W. Hrubesh and J.F. Poco, 'Aerogel films for optical, thermal, acoustic and electronic applications', submitted to J. Non-Cryst. Solids.

[2] S.S. Kistler, Nature 127 (1931) 741.

[3] C.J. Brinker and G.W. Scherer, Sol–Gel Science: The Physics and Chemistry of Sol–Gel Processing (Academic Press, San Diego, CA, 1990).

[4] R. Deshpande, D.M. Smith and C.J. Brinker, US patent application (1992).

[5] D.J. Stein, A. Maskara, S. Hærid, J. Anderson and D.M. Smith, in: Better Ceramics Through Chemistry VI, ed. A.K. Cheetham, C.J. Brinker, M.L. Mecartney and C. Sanchez, Mater. Res. Soc. Symp. Proc., Vol. 346 (Materials Research Society, Pittsburgh, PA, 1994) p. 643.

[6] D.M. Smith, R. Deshpande and C.J. Brinker, in: Better Ceramics Through Chemistry V, ed. M.J. Hampden-Smith, W.G. Klemperer and C.J. Brinker, Mater. Res. Soc. Symp. Proc., Vol. 271 (Materials Research Society, Pittsburgh, PA, 1992) p. 567.

[7] A.J. Hurd and C.J. Brinker, J. Phys. (Paris) 49 (1988) 1017.

[8] A.J. Hurd and C.J. Brinker, in: Better Ceramics Through Chemistry III, ed. C.J. Brinker, D.E. Clark and D.R. Ulrich, Mater. Res. Soc. Symp. Proc., Vol. 121 (Materials Research Society, Pittsburgh, PA, 1988) p. 731.

[9] E.P. Plueddemann, Silane Coupling Agents (Plenum, New York, 1991).

[10] C.J. Brinker and S.S. Prakash, US patent disclosure (1994).

[11] S.S. Prakash, C.J. Brinker and A.J. Hurd, unpublished.

[12] C.J. Brinker, A.J. Hurd, G.C. Frye, P.R. Schunk and C.S. Ashley, The Centennial Memorial Issue of The Ceramic Society of Japan 99 (10) (1991) p. 862.

[13] R.M.A. Azzam and N.M. Bashara, Ellipsometry and Polarized Light (North-Holland, Amsterdam, 1987).

[14] L.J. Bellamy, The Infra-Red Spectra of Complex Molecules (Wiley, New York, 1975).

[15] S.S. Prakash, C.J. Brinker, A.J. Hurd and S.M. Rao, Nature 374 (1995) 439.

[16] D.M. Smith, J. Anderson and D.J. Stein, 'Preparation of low-density aerogels at ambient pressure', submitted to J. Non-Cryst. Solids.